Electronic Supplementary Information

Three in One: Engineering MOF Channels via Coordinated Water Arrays for Regulated Separation of Alkanes and Alkenes†

Lu-Lu Ma,[a,b] Pavel N. Zolotarev,[c] Kang Zhou,[b] Xin Zhou,[b] Jiaqi Liu,[b] Jiafeng Miao,[b] Shenfang Li,[b] Guo-Ping Yang,*[a] Yao-Yu Wang,[a] Davide M. Proserpio,*[c] Jing Li,*[d,c] Hao Wang*[b]

[a]Key Laboratory of Synthetic and Natural Functional Molecule Chemistry of the Ministry of Education, Shaanxi Key Laboratory of Physico-Inorganic Chemistry, College of Chemistry & Materials Science, Northwest University, Xi'an 710127, P. R. China. E-mail: ygp@nwu.edu.cn

[b]Hoffmann Institute of Advanced Materials, Shenzhen Polytechnic 7098 Liuxian Blvd., Nanshan District, Shenzhen, Guangdong 518055, P. R. China. E-mail: wanghao@szpt.edu.cn

[c]Dipartimento di Chimica, Università degli Studi di Milano, 20133 Milano, Italy. Email: davide.proserpio@unimi.it

[d]Department of Chemistry and Chemical Biology, Rutgers University, 123 Bevier Road, Piscataway, New Jersey 08854, United States. Email: jingli@rutgers.edu

Supplementary Methods

Search for isoreticular rod-MOFs. The TopCryst service contains the data on the representatives of different topological types of all coordination networks collected in the CSD. The nets stored in the service are the result of the standard and cluster representation obtained using an automatic procedure, which guarantees rigor of the analysis and the coverage of the large amount of data. With these advantages comes the disadvantage, the rod-MOF representations are not stored because their construction requires user intervention in an *ad hoc* manner. Therefore, for the search of the analogous/isoreticular rod-net MOFs a workaround has been employed. First, we obtained the *standard representation* for **HIAM-317** in which metal atoms and ligand's center of mass serve as network nodes that results in the 6,8-connected **sea** net. The search in the TopCryst service revealed 42 structures of **sea** topological type, but not all 42 structures are rod-MOF, so we need to find those that can be described with the same rod net as in **HIAM-317**. We have applied the algorithm reported in [L. S. Xie, E. V. Alexandrov, G. Skorupskii, D. M. Proserpio and M. Dincă, Chem. Sci., 2019, 10, 8558–8565] to find the *point of extension and metal* (PE&M) description for **HIAM-317**, which results in the underlying net of the 3,4,6T325 topological type. We have obtained the PE&M representation for the 42 structures with **sea** topology and found that 26 of them are rod-MOF isoreticular with **HIAM-317** (see Table S3). A manual check of 26 structures, revealed that only the HIQLEB structure (UPC-101-Al) [Weidong Fan, Xia Wang, Ben Xu, Yutong Wang, Dandan Liu, Ming Zhang, Yizhu Shang, Fangna Dai, Liangliang Zhang, Daofeng Sun, Journal of Materials Chemistry A, 2018, 6, 24486, DOI: 10.1039/C8TA07839D] comprises the ligand most similar to the one in **HIAM-317**.

The standard **sea** or the PE&M 3,4,6T325 are not the best nets for a good visual description of Y-MOF, so we also computed the straight rod (STR) net. In the STR representation the biphenyl core of the tetratopic ligand was represented as two linked 3-connected nodes and the rods comprise carboxylate-connected yttrium atoms. From the figure below two –COO groups are pointing to Y and each Y is bridged to the next Y by an oxygen atom of the bridging OH and another bridge comes from one oxygen of the carboxylates.
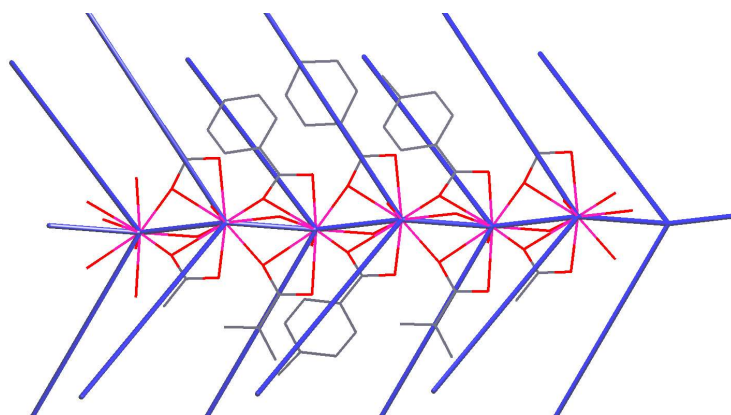
The unnecessary bonds between carboxylates and yttrium atoms were deleted, and after simplification the rods appear as a zig-zag chain of nodes. Each of these nodes is now 4-coordinated, linked to two PEs (the C atom of the carboxylate) attributed to two different ligands, in addition to two other nodes of the rod. The 3,4-coordinated net obtained in such way corresponds to the **jeb** topological type (see the figure above and S7b).

General characterizations

All reagents were obtained from commercial sources and used without further purification. Single crystal X-ray diffraction data were collected on a 'Bruker D8 VENTURE' diffractometer. The data of **HIAM-317** and **HIAM-317a** were collected using MoKα (λ = 0.71073 Å) and CuKα (λ = 1.5406 Å), respectively. Using Olex2, the structures were solved with the ShelXT structure solution program using Intrinsic Phasing and refined with the ShelXL refinement package using Least Squares minimization. Powder X-ray diffraction patterns were recorded on a Bruker D8 Advance with Cu Kα radiation (λ= 1.5406 Å). Data were collected at room temperature at 2θ = 3 ~ 40°. Thermogravimetric measurements were performed on a thermal analyzer (TGA 550, TA Instruments) in N_2 atmosphere and the ramping rate was 10 °C/min. Scanning electron micrographs (SEM) images were taken using a JEOL JSM-IT800 (SHL). X-ray Photoelectron Spectroscopy (XPS) (including high-resolution spectrum) data were collected on Thermo Fisher ESCALAB 250Xi. C_2H_4, and C_2H_6 adsorption isotherms were measured on a Micromeritics 3Flex analyzer, while C_3H_6, and C_3H_8 adsorption isotherms were measured on a BSD-660. For each adsorption experiment, ~100 mg of MOF sample was activated 12 hours prior to data collection.

Synthesis of HIAM-317

H_4TCHB (20 mg, 0.03 mmol), 2-fluorobenzoic acid (500 mg, 3.57 mmol), $Y(NO_3)_3 \cdot 6H_2O$ (40.0 mg,

0.10 mmol), DMF (4 mL), and H_2O (4 mL) were combined in a 20 mL Teflon bomb (Xi'an Taikang Technology Co., Ltd.) and the mixture was heated at 130 °C for 72 hours. After cooling down to room temperature, the obtained crystals were washed by DMF and then exchanged with CH_2Cl_2 3 times daily for 3 days. The solvent-exchanged samples were directly activated at 120 °C or 300 °C under dynamic vacuum for 12 hours to yield activated samples.

Breakthrough measurements

Breakthrough experiments were carried out in an auto mixed-gas breakthrough apparatus mixSorb S (manufactured by 3P Instruments and distributed by JWGB Instruments) equipped with a mass spectrum (MKS Circus 3). 1.58 g of adsorbent was packed into a steel column (I.D. 4 mm, volume 1 ml) and was activated at 120 or 300 °C for 4 hours under helium purging (10 ml/min) prior to measurements. When the temperature was cooled down to 25 °C, helium flow was stopped and the feed mixed gases at a flow rate of 1 mL/min were introduced to the adsorption column. The outlet gas was analyzed using a mass spectrometer. After the adsorption reached dynamic equilibrium, the column was purged with helium (10 mL/min) at 120 °C for 1 hour for regeneration.

Fitting adsorption heat of pure component isotherms

$$\ln P = \ln N + 1/T\sum_{i=0}^{m} a_i N^i + \sum_{i=0}^{n} b_i N^i \tag{1}$$

$$Q_{st} = -R\sum_{i=0}^{m} a_i N^i \tag{2}$$

The above virial expression was used to fit the combined isotherm data for **HIAM-317b** at 273 and 298 K (P is the pressure, N is the adsorbed amount, T is the temperature, a_i and b_i are virial coefficients, and m and N are the number of coefficients used to describe the isotherms). Q_{st} is the coverage-dependent enthalpy of adsorption and R is the universal gas constant.

Selectivity prediction via IAST

The experimental isotherm data for pure gas A, and gas B were fitted at 273 and 298 K using a Langmuir-Freundlich (L-F) model:

$$q = \frac{a_1 * b_1 * P^{c_1}}{1 + b_1 * P^{c_1}} + \frac{a_2 * b_2 * P^{c_2}}{1 + b_2 * P^{c_2}} \tag{3}$$

Where q and p were adsorbed amounts and the pressure of component i, respectively.

The adsorption selectivities for binary mixtures of gas A/gas B, defined by

4

$$S_{i/j} = \frac{x_i * y_j}{x_j / y_i} \tag{4}$$

were respectively calculated using the Ideal Adsorption Solution Theory (IAST) of Myers and Prausnitz. Where x_i is the mole fraction of component i in the adsorbed phase and y_i is the mole fraction of component i in the bulk.

Ab initio calculations and simulation details.

We used the DFT as implemented in the Vienna *Ab initio* simulation package (VASP) in all calculations. The exchange-correlation potential is described by using the generalized gradient approximation of Perdew-Burke-Ernzerhof (GGA-PBE). The projector augmented-wave (PAW) method is employed to treat interactions between ion cores and valence electrons. The plane-wave cutoff energy was fixed to 500 eV. Given structural models were relaxed until the Hellmann–Feynman forces smaller than -0.02 eV/Å and the change in energy smaller than 10^{-5} eV was attained. During the relaxation, the Brillouin zone was represented by a Γ centered k-point grid of $10 \times 10 \times 1$. Grimme's DFT-D3 methodology was used to describe the dispersion interactions among all the atoms in adsorption models. And we used pymatgen to simulate the adsorption sites of the structure.

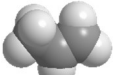**Table S1.** Comparison for molecular sizes and physical properties of C_2H_4, C_2H_6, C_3H_6 and C_3H_8.
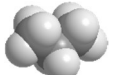
Compounds	Ball and Stick model	Dimensions (10^{-10} m)	Kinetic Diameter (10^{-10} m)	Boiling point (K)
C_2H_4		3.28×4.18×4.84	4.2	169.5
C_2H_6		3.81×4.08×4.82	4.4	184.6
C_3H_6		4.65×4.16×6.44	4.6	225.45
C_3H_8		4.20×4.60×6.80	4.3	231.05

Table S2. Crystallographic data for **HIAM-317** and **HIAM-317a**.

Compound	HIAM-317	HIAM-317a
Chemical formula	$C_{23}H_{20}O_6Y$	$C_{23}H_{20}O_6Y$
Formula weight	481.30	481.30
T (K)	200 K	253 K
Radiation (Å)	MoKα (λ = 0.71073)	CuKα (λ = 1.54178)
Crystal system	Orthorhombic	Orthorhombic
Space group	*Ibam*	*Ibam*
a, b, c (Å)	6.7432(2), 24.8499(9), 31.0273(11)	6.7374(7), 24.870(3), 30.881(4)
$α, β, γ$ (°)	90, 90, 90	90, 90, 90
V (Å^3)	5199.2(3)	5174.4(10)
Z	8	8
Density (calculated) (g cm^{-3})	1.230	1.236
$μ$ (mm^{-1})	2.273	3.443
Reflections collected / unique / R_{int}	28731 / 2736 / 0.1079	10327 / 2151 / 0.2428
Goodness-of-fit on F^2	1.045	1.010
R_1[a], wR_2[b] (I > 2σ)	0.0392 / 0.0951	0.0982 / 0.2399
R_1[a], wR_2[b] (all data)	0.0558 / 0.1032	0.1308 / 0.2661

[a]$R_1 = Σ||F_o| − |F_c||)/Σ|F_o|$; [b]$wR_2 = [Σw(F_o^2 − F_c^2)^2/Σw(F_o^2)^2]^{1/2}$

Table S3. Selected bond lengths (Å) and angles (°) for **HIAM-317**.

Y(1)-Y(1)#1	3.5839(3)	Y(1)-O(2)	2.355(2)
Y(1)-O(1)#2	2.317(3)	Y(1)-O(2)#4	2.437(2)
Y(1)-O(1)	2.258(3)	Y(1)-O(3)	2.336(4)
Y(1)-O(2)#2	2.437(2)	Y(1)-O(4)#2	2.475(2)
Y(1)-O(2)#3	2.355(2)	Y(1)-O(4)#4	2.475(2)
O(1)#2-Y(1)-Y(1)#1	102.52(7)	O(2)#3-Y(1)-Y(1)#1	42.46(5)
O(1)-Y(1)-Y(1)#1	39.02(8)	O(2)#2-Y(1)-Y(1)#1	144.85(5)
O(1)-Y(1)-O(1)#2	141.55(9)	O(2)#3-Y(1)-O(2)#4	145.90(5)
O(1)#2-Y(1)-O(2)#3	77.84(8)	O(2)#3-Y(1)-O(2)#2	103.04(7)
O(1)#2-Y(1)-O(2)	77.84(8)	O(2)-Y(1)-O(2)#4	103.04(7)
O(1)-Y(1)-O(2)#3	70.48(9)	O(2)#3-Y(1)-O(2)	67.87(10)
O(1)-Y(1)-O(2)#2	139.62(7)	O(2)-Y(1)-O(2)#2	145.90(5)
O(1)-Y(1)-O(2)#4	139.62(7)	O(2)#2-Y(1)-O(2)#4	65.30(9)
O(1)-Y(1)-O(2)	70.48(9)	O(2)#3-Y(1)-O(4)#4	138.39(8)
O(1)#2-Y(1)-O(2)#4	68.07(8)	O(2)#4-Y(1)-O(4)#4	52.56(7)
O(1)#2-Y(1)-O(2)#2	68.07(8)	O(2)#3-Y(1)-O(4)#2	71.23(8)
O(1)#2-Y(1)-O(3)	139.41(12)	O(2)-Y(1)-O(4)#2	138.39(8)
O(1)-Y(1)-O(3)	79.04(13)	O(2)#2-Y(1)-O(4)#2	52.56(7)
O(1)-Y(1)-O(4)#4	89.11(6)	O(2)#2-Y(1)-O(4)#4	115.18(7)
O(1)-Y(1)-O(4)#2	89.11(6)	O(2)-Y(1)-O(4)#4	71.24(8)
O(1)#2-Y(1)-O(4)#2	101.00(7)	O(2)#4-Y(1)-O(4)#2	115.18(7)
O(1)#2-Y(1)-O(4)#4	101.00(7)	O(3)-Y(1)-Y(1)#1	118.06(10)
O(2)#4-Y(1)-Y(1)#1	144.85(5)	O(3)-Y(1)-O(2)#4	78.04(10)
O(2)-Y(1)-Y(1)#1	42.46(5)	O(3)-Y(1)-O(2)#2	78.04(10)
O(3)-Y(1)-O(2)#3	133.00(9)	O(4)#4-Y(1)-Y(1)#1	99.72(5)
O(3)-Y(1)-O(2)	133.00(9)	O(4)#2-Y(1)-O(4)#4	146.56(13)
O(3)-Y(1)-O(4)#4	73.44(7)	Y(1)-O(1)-Y(1)#1	103.14(13)
O(3)-Y(1)-O(4)#2	73.44(7)	Y(1)-O(2)-Y(1)#1	96.82(7)
O(4)#2-Y(1)-Y(1)#1	99.72(5)		

Symmetry transformations used to generate equivalent atoms: #1 x-1/2, -y+3/2, -z+1; #2 x+1/2, -y+3/2, -z+1; #3 x, y, -z+1; #4 x+1/2, -y+3/2, z; #5 -x+1, -y+1, z; #6 -x+1, y, -z+1/2.

Table S4. The 26 isoreticular structures with 3,4,6T325 PE&M underlying net observed in **HIAM-317**.

refcode	composition	Space Group	Name
GUKVEO	C10 H4 Al2 O10	Pbam	(mu8-Benzene-1,2,4,5-tetracarboxylato)-bis(mu2-hydroxo)-di-aluminium) MIL-118B
GUKVIS	C10 H9.5 Al2 O12.75	Pnam	(mu8-Benzene-1,2,4,5-tetracarboxylato)-bis(mu2-hydroxo)-di-aluminium hydrate) MIL-118C
GUXQAR	C10 H12 O14 V2	P-1	(mu8-1,2,4,5-Benzenetetracarboxylato)-bis(mu2-hydroxo)-di-vanadium(iii) tetrahydrate) MIL-60
HALTUM	C60 H60 N4 Ni4 O22	P21/m	bis(mu-1,1':4',1"-terphenyl-2',4,4",5'-tetracarboxylato)-bis(mu-N,N-dimethylacetamide)-bis(mu-aqua)-tetra-nickel N,N-dimethylacetamide solvate
HERYOT	C14 H8 O10 Zn2	Pbam	(mu8-1,4,5,8-Naphthalenetetracarboxylato)-di-aqua-di-zinc)
HIQLEB	C40 H31 Al2 N2 O12.5	Cmmm	bis(mu-hydroxo)-(mu-3,3',5,5'-tetrakis(4-carboxylatophenyl)[1,1'-biphenyl-4,4'-diamine)-di-aluminium(iii) hydrate UPC-101-Al
LURRUM	C53 H53 In2 N3 O17	Cmmm	mu8-4,4',4",4"'-(Pyrene-1,3,6,8-tetrayl)tetrabenzoato)-bis(mu2-hydroxo)-di-indium(iii) dimethylformamide solvate tetrahydrate
NUFYAP	C28 H12 Al4 O20	P21/c	bis(mu8-1,4,5,8-Naphthalenetetracarboxylato)-tetrakis(mu2-hydroxo)-tetra-aluminium)
NUFYET	C14 H6 Ga2 O10	P21/c	(mu8-1,4,5,8-Naphthalenetetracarboxylato)-bis(mu2-hydroxo)-di-gallium)
NUFYIX	C14 H6 In2 O10	P21/c	(mu8-1,4,5,8-Naphthalenetetracarboxylato)-bis(mu2-hydroxo)-tetra-indium)
QUCFUR	C16 H10 Al2 O13 S1	P-1	mu8-4,4'-Sulfonyldibenzene-1,2-dicarboxylato)-bis(mu2-hydroxo)-di-aluminium monohydrate CAU-12-dehy
RAYYOI	C48 H33.1 Al2 Co1 N4 O13.55	Cmmm	mu-5,10,15,20-tetrakis(4-carboxylatophenyl)porphyrinato)-bis(mu-hydroxo)-di-aluminium-cobalt hydrate
SULZOR	C24 H10 O10 Sc2	P21/c	bis(mu-hydroxo)-(mu-perylene-3,4,9,10-tetracarboxylato)-di-scandium) Sc-CAU-9-PTCDA
SUMBAG	C34 H22 O11 Sc2	Cmmm	(mu-1,2,4,5-tetrakis(4-carboxylatophenyl)benzene)-bis(mu-hydroxo)-

			di-scandium hydrate) Sc-CAU-9-TCPB
TAPCIX	C14 H8 Mn2 O10	Pbam	mu8-Naphthalene-1,4,5,8-tetracarboxylato)-bis(mu2-aqua)-di-manganese(ii)
UMARIL	C60 H60 Mg4 N4 O22	P21/n	bis(mu8-1,1':4',1"-Terphenyl-2',4,4",5'-tetracarboxylato)-bis(mu2-aqua)-bis(mu2-dimethylacetamide)-tetra-magnesium dimethylacetamidesolvate)
VUFJUE	C48 H24 Fe2 N4 Ni1 O10	Cmmm	mu-4,4',4",4"'-(porphyrin-5,10,15,20-tetrayl)tetrabenzoato)-bis(mu-oxo)-di-iron(iii)-nickel(ii) unknown solvate
VUFRIA	C48 H26 Cu1 Fe2 N4 O10	Cmmm	bis(mu-hydroxo)-(mu-4,4',4",4"'-(porphyrin-5,10,15,20-tetrayl)tetrabenzoato)-copper-di-iron unknown solvate) Cu-PMOF-3(Fe)
WIXKOG	C32 H18 Ga2 N2 O10	Cmmm	mu-2,3,5,6-tetrakis(4-carboxylatophenyl)pyrazine)-bis(mu-hydroxo)-di-gallium unknown solvate
XAJQAC	C58.7 H40.8 In2 O10	P2/c	mu8-4,4',4",4"'-(Pyrene-1,3,6,8-tetrayl)tetrabenzoato)-bis(mu2-hydroxo)-di-indium(iii) toluene solvate
XIHWUI	C64 H60 Mn4 N4 O22	P21/c	bis(mu8-1,1':4',1"-Terphenyl-2',4,4",5'-tetracarboxylato)-bis(mu2-1-methylpyrrolidin-2-one)-bis(mu2-aqua)-tetra-manganese(ii)bis(1-methylpyrrolidin-2-one))
XIHXAP	C60 H60 Mn4 N4 O22	P21/c	bis(mu8-1,1':4',1"-Terphenyl-2',4,4",5'-tetracarboxylato)-bis(mu2-N,N-dimethylacetamide)-bis(mu2-aqua)-tetra-manganese(ii)N,N-dimethylacetamide solvate)
XIHXAP01	C60 H60 Mn4 N4 O22	P21/n	bis(mu8-1,1':4',1"-Terphenyl-2',4,4",5'-tetracarboxylato)-bis(mu2-N,N-dimethylacetamide)-bis(mu2-aqua)-tetra-manganese(ii)N,N-dimethylacetamide solvate)
XIXCIT	C50 H40 Ca2 N2 O12	Pbam	bis(mu-aqua)-(mu-4,4',4",4"'-(pyrene-1,3,6,8-tetrayl)tetrabenzoato)-di-calcium N,N-dimethylformamide solvate SION-8
XIXCIT01	C44 H26 Ca2 O10	Pbam	mu-4,4',4",4"'-(pyrene-1,3,6,8-tetrayl)tetrabenzoato)-bis(mu-aqua)-di-calcium unknown solvate ECUT-50
XOCROY	C12 H8 Al2 O16	Cmcm	mu8-1,4-dicarboxybenzene-2,3,5,6-tetracarboxylato)-bis(mu2-hydroxo)-di-aluminium dihydrate

Table S5. Fitting parameters of Clausius-Clapeyron isotherm model.

	C_2H_4	C_2H_6	C_3H_6	C_3H_8
a_0	-2713.86452	-2890.50882	-5934.47367	-5050.18038
a_1	4.84593	-2.522	24.50682	17.89267
a_2	0	0.18538	-0.7099	0
a_3	0	-0.00411	0.0086	0
a_4	0	6.88127E-5	-2.65842E-5	0
a_5	0	-3.50807E-7	0	0
b_0	10.97584	11.12985	18.55703	14.06149
Chi^2	5.25118E-5	3.51159E-5	0.04394	0.14364
R^2	0.99838	0.99999	0.97922	0.94557

Table S6. Fitting parameters of Dual-site Langmuir-Freundlich isotherm model.

	C_2H_4	C_2H_6	C_3H_6	C_3H_8	T (K)
a_0	2.29687	1.97407	1.7193	3.29593	273
b_1	0.02718	0.04994	0.01978	0.01138	273
c_1	1.12517	1.17578	0.95261	1.00967	273
a_2	12.7428	10.83435	2.15593	0.03324	273
b_2	0.00225	0.00432	0.00116	6.79306E-5	273
c_2	0.62794	0.57792	1.48208	2.78521	273
Chi^2	4.65549E-6	3.5282E-6	1.59273E-6	5.73621E-7	273
R^2	0.9999	0.9999	0.9999	0.9999	273
a_0	2.11429	0.29386	0.067	0.23411	298
b_1	0.81647	0.01353	8.63816E-8	0.00345	298
c_1	1.16375	1.91403	4.58816	2.38034	298
a_2	0.33265	1.72784	2.09881	1.49042	298
b_2	0.00842	1.51	0.23671	0.54461	298
c_2	1.63051	1.07374	1.08093	1.14268	298
Chi^2	1.21097E-5	1.91581E-5	1.08093	5.25944E-5	298
R^2	0.9999	0.9999	0.9999	0.999	298

Fig. S1 Optical microscope image of the as-synthesized crystals of **HIAM-317**.
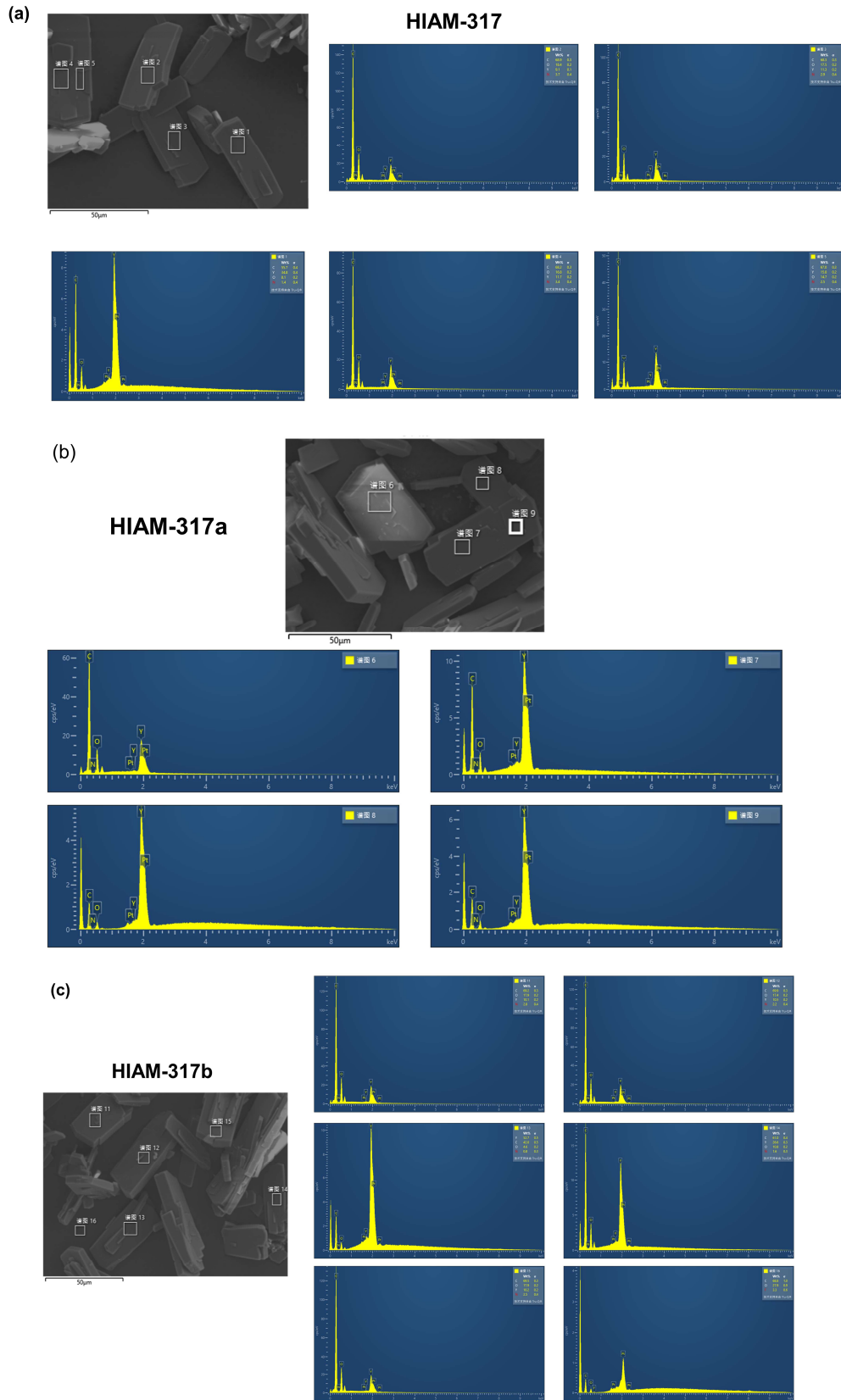
Fig. S2 The SEM and SEM-EDX patterns for **HIAM-317** (a), **HIAM-317a** (b), and **HIAM-317b** (c).

TEM

SAED patterns

HIAM-317 **HIAM-317a** **HIAM-317b**
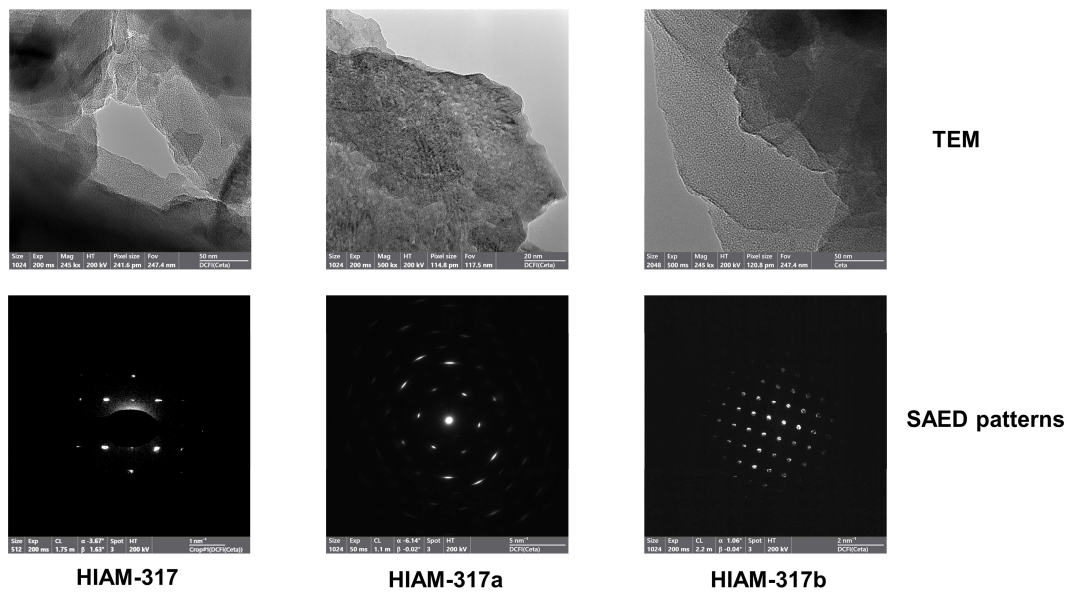
Fig. S3 The TEM and SAED patterns for **HIAM-317**, **HIAM-317a**, and **HIAM-317b**.
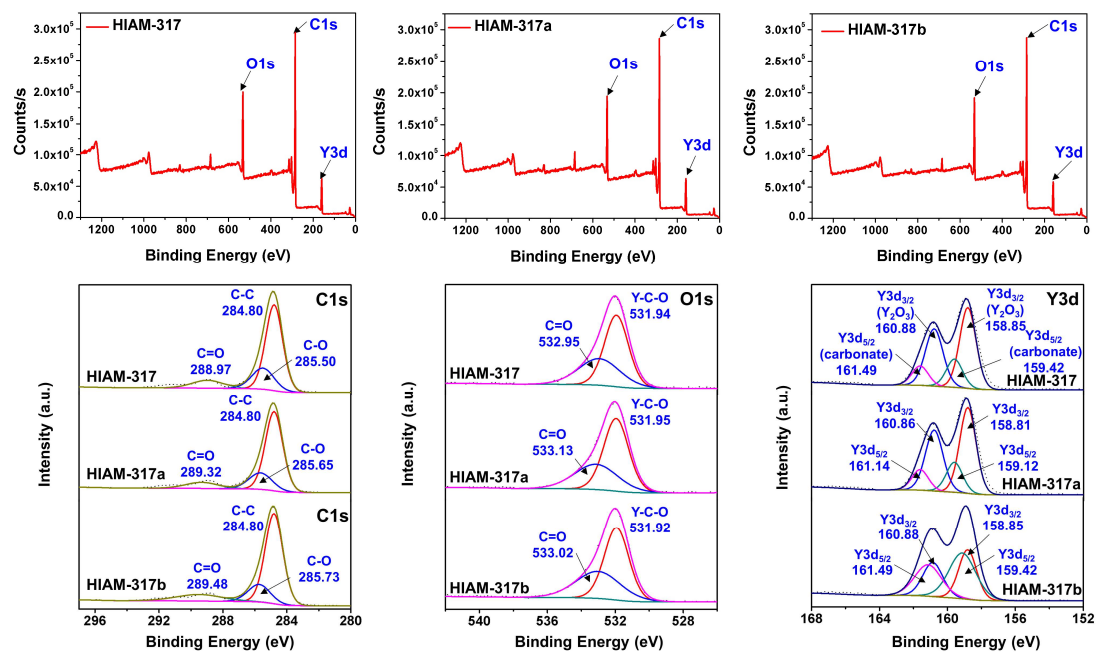
Fig. S4 The XPS spectra (including high-resolution spectrum) for HIAM-317, HIAM-317a and HIAM-317b.
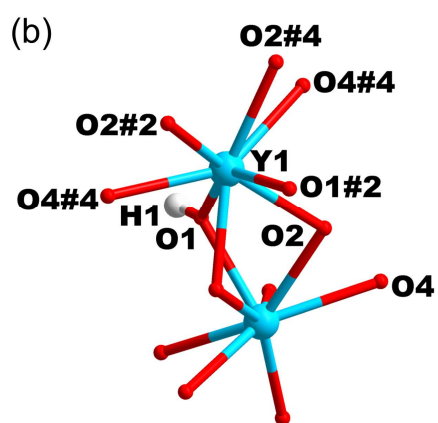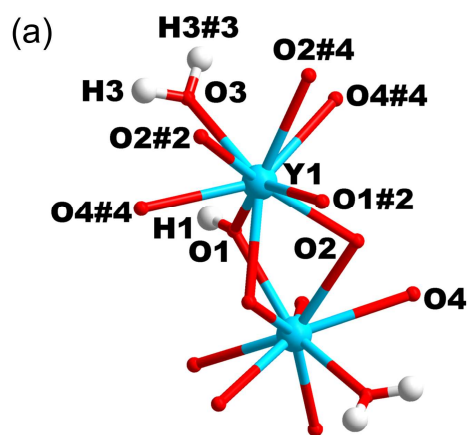
Fig. S5 The coordination mode of **HIAM-317a** and **HIAM-317b**. (Symmetric code: #2 = 1/2+x, 3/2-y, 1-z; #3 = x, y, 1-z; #4 = 1/2+x, 3/2-y, z)
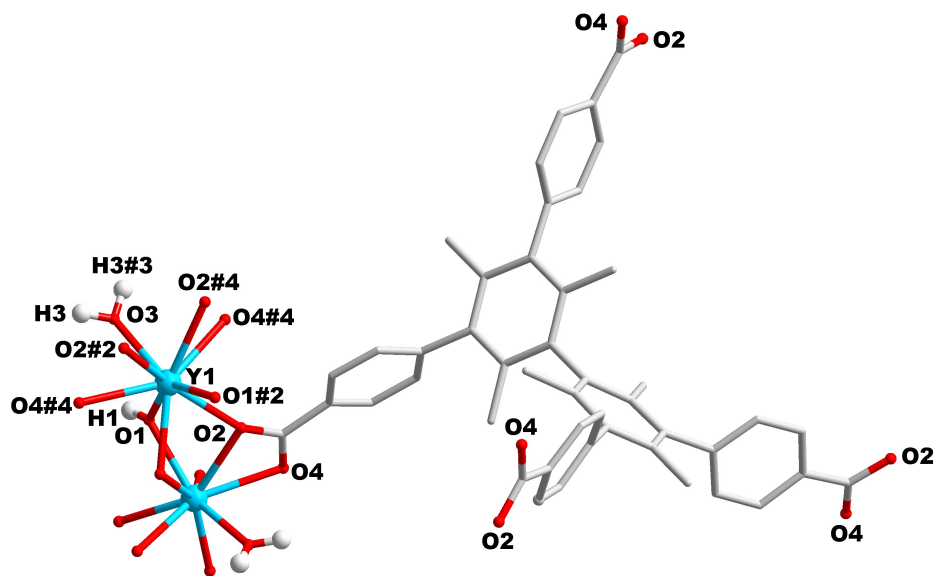
Fig. S6 The asymmetric unit of **HIAM-317**. (Symmetric code: #2 = 1/2+x, 3/2-y, 1-z; #3 = x, y, 1-z; #4 = 1/2+x, 3/2-y, z)
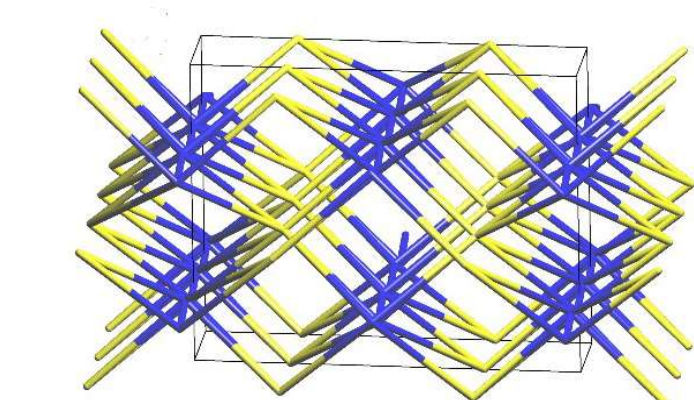
a) **6,8-c sea**
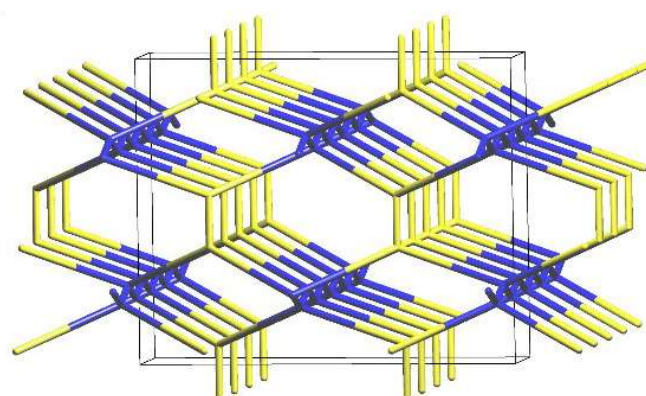
b) **3,4-c jeb**
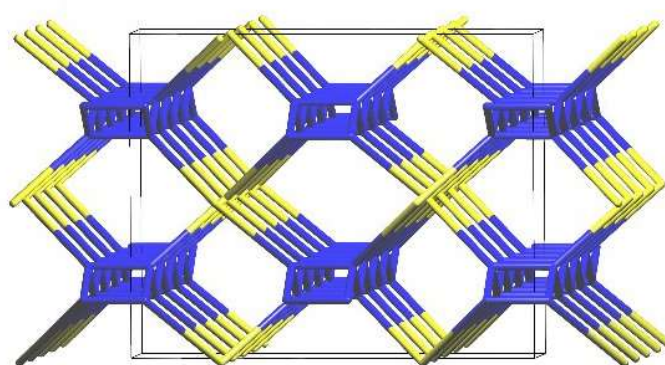
c) **4,4-c frl**

Fig. S7 The topological representations of **HIAM-317**.
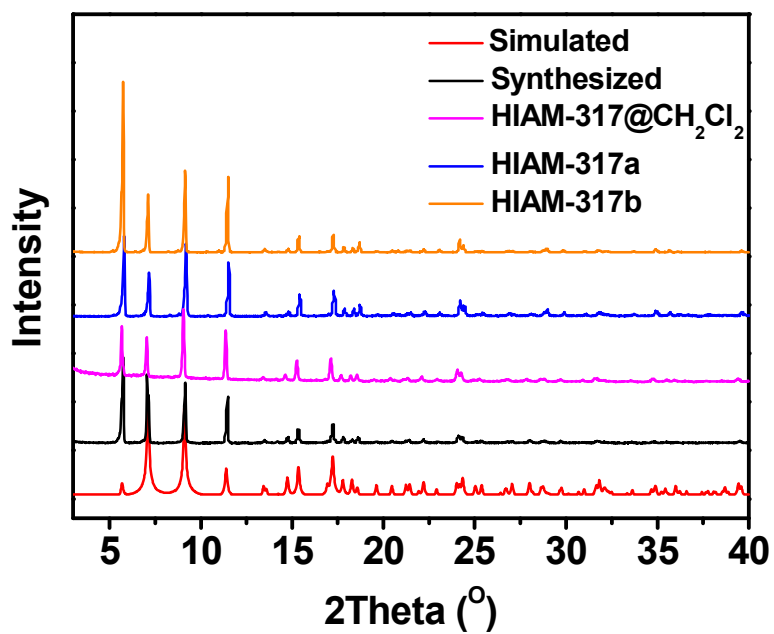
Fig. S8 Simulated and experimental PXRD patterns of **HIAM-317** in different forms.
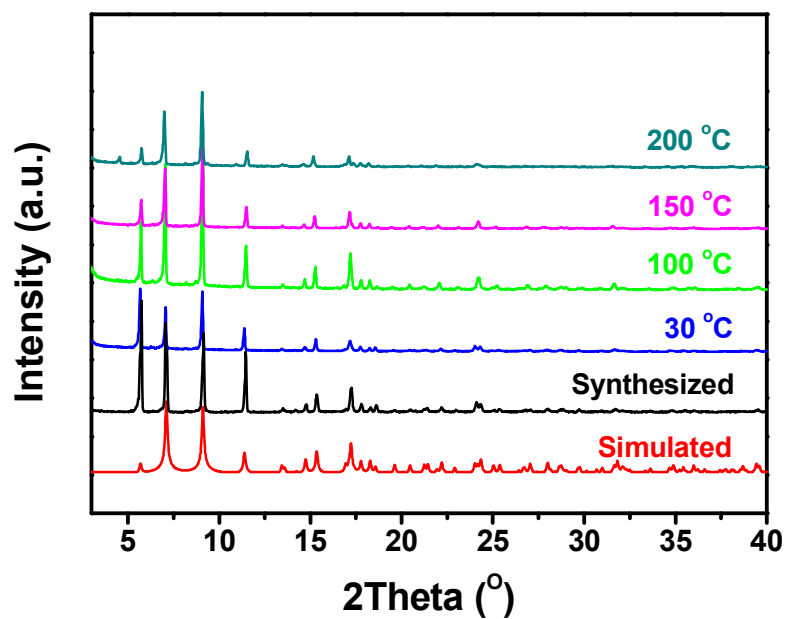
Fig. S9 In-situ PXRD patterns of **HIAM-317** collected at different temperatures and under ambient air atmosphere.
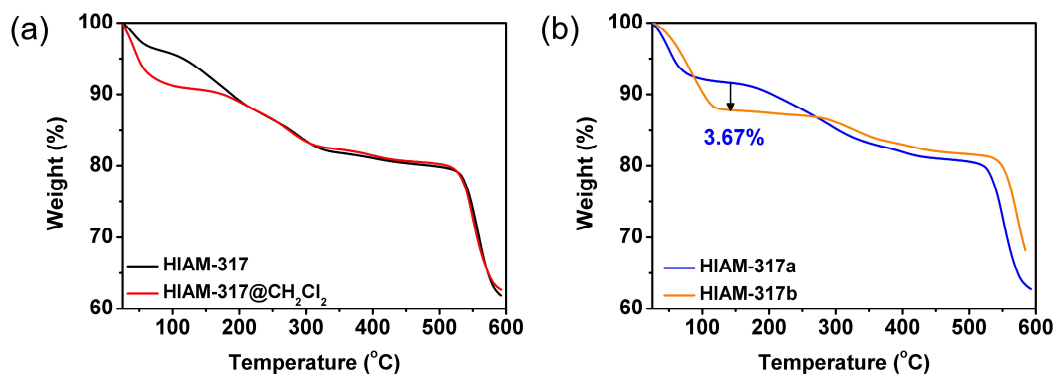
Fig. S10 (a) TGA curves of as-synthesized and CH$_2$Cl$_2$-exchaned samples of **HIAM-317**; (b) TGA curves of **HIAM-317a** and **HIAM-317b**.
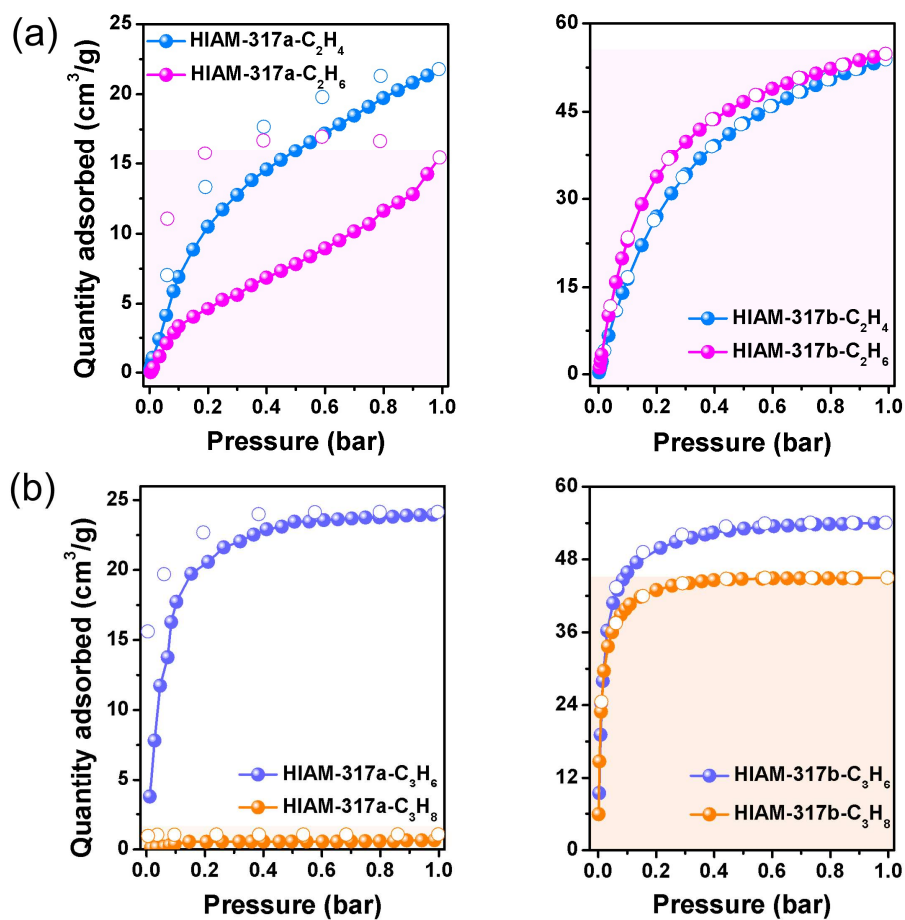
Fig. S11 Adsorption isotherms of C_2H_4 and C_2H_6 (a) and C_3H_6 and C_3H_8 (b) for **HIAM-317a** and **HIAM-317b** at 273 K.
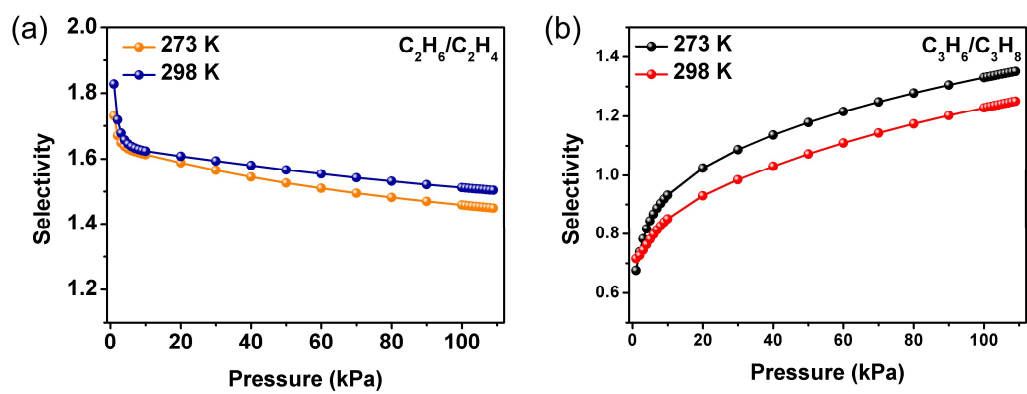
Fig. S12 IAST selectivity of **HIAM-317b** for equimolar binary C_2H_6/C_2H_4 (a) and C_3H_6/C_3H_8 (b) mixtures at 273 and 298 K.
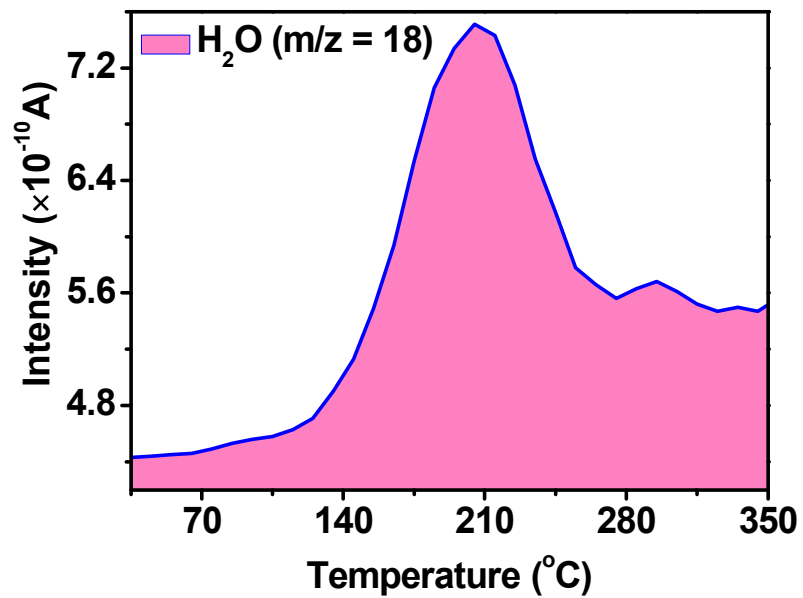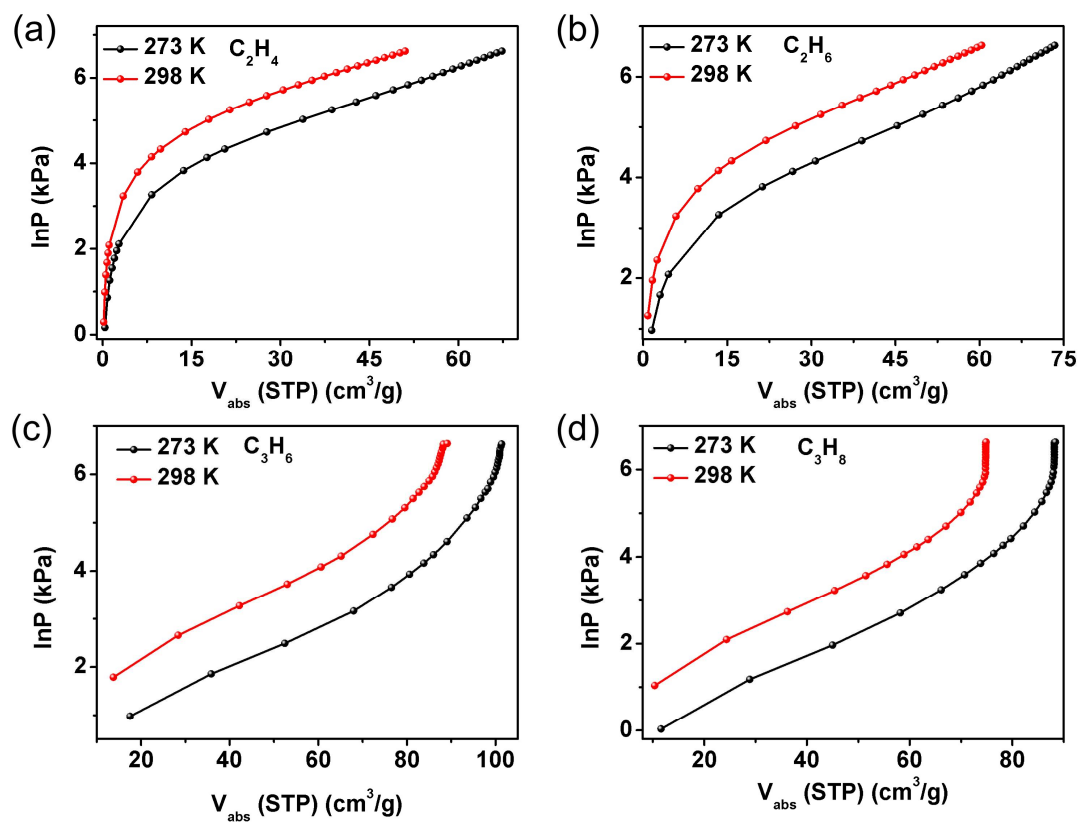
Fig. S13 TG-MS curve of CH_2Cl_2@**HIAM-317**.

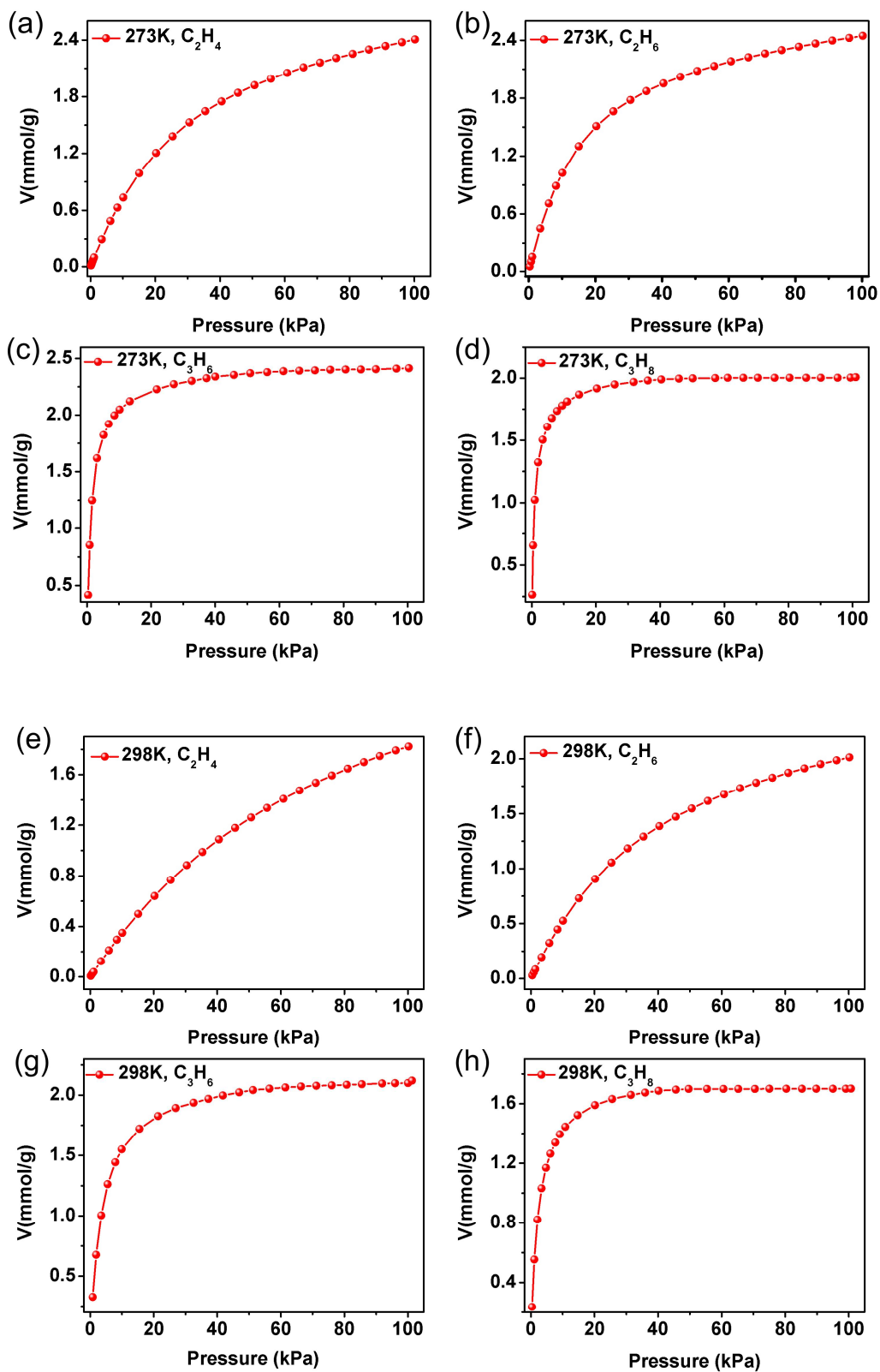**Fig. S14** Fitted adsorption isotherms of C_2H_4 (a), C_2H_6 (b), C_3H_6 (c) and C_3H_8 (d) for **HIAM-317b**.

Fig. S15 Fitted adsorption isotherms of C_2H_4, C_2H_6, C_3H_6 and C_3H_8 at 273 K (a)-(d) and 298 K (e)-(h) for **HIAM-317b**.
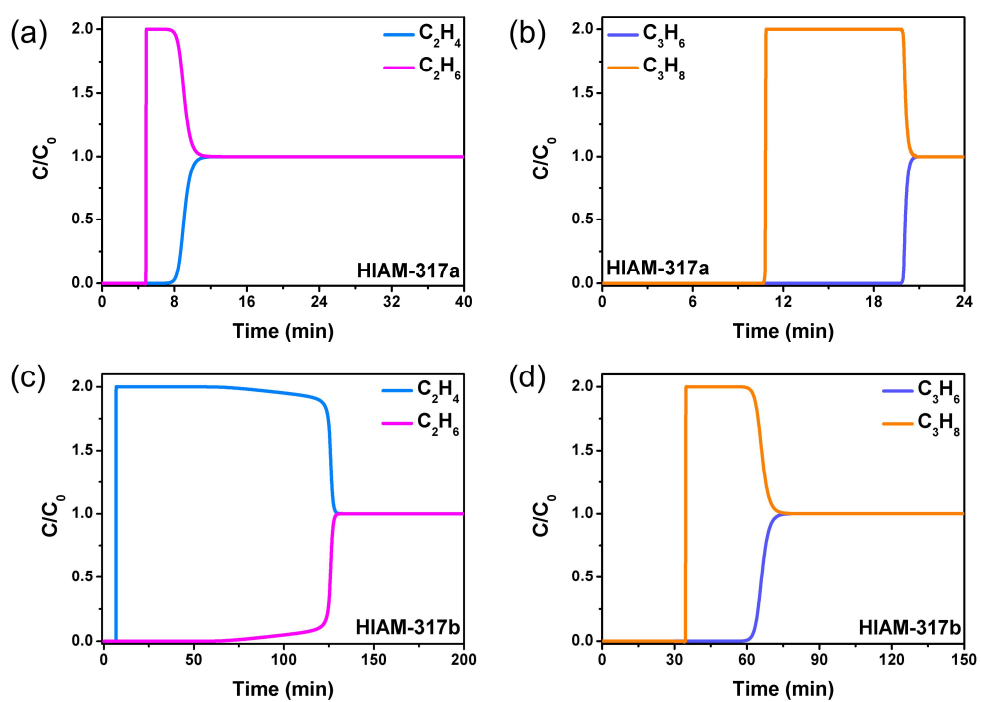
Fig. S16 Simulation of breakthrough experiments for C_2H_4/C_2H_6 (v/v, 1/1) and C_3H_6/C_3H_8 (v/v, 1/1) on **HIAM-317a** and **HIAM-317b** at 298K and 100 kPa.
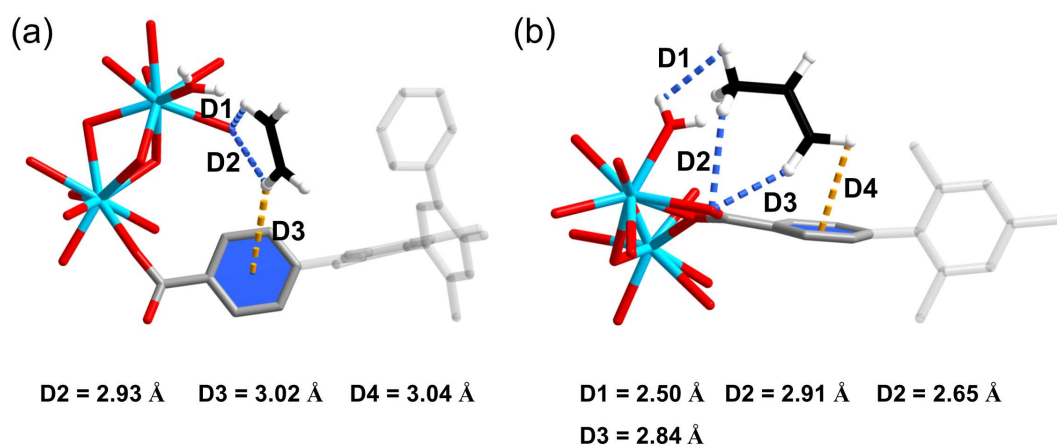
Fig. S17 The preferential adsorption sites of **HIAM-317a** for C_2H_4 (a) and C_3H_6 (b). The C-H···π and C-H···O interations are prestented by orange and orange dashed line respectivily.
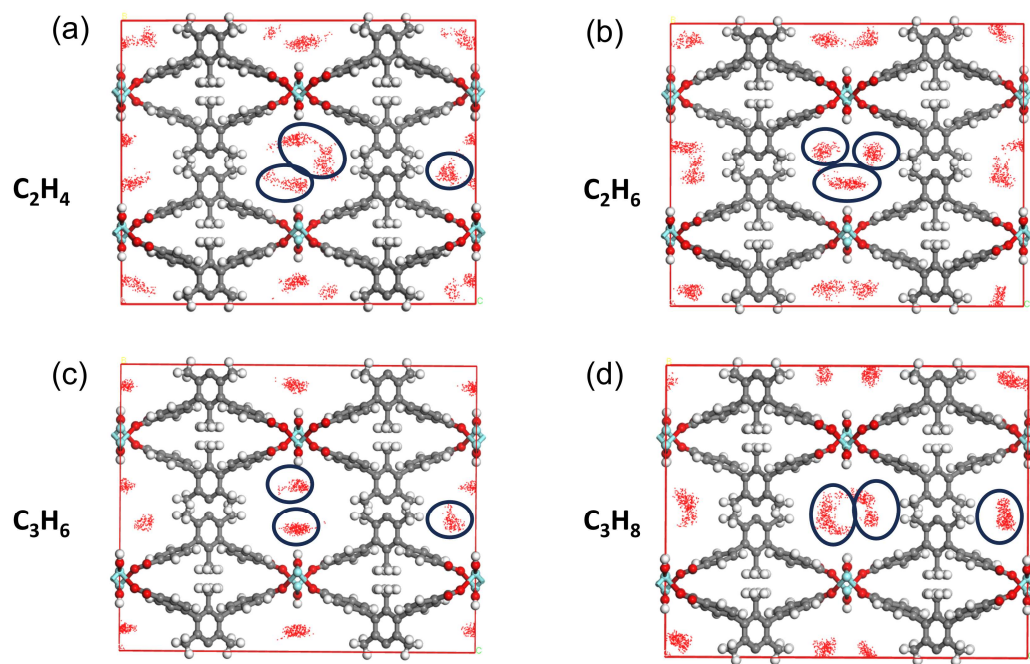
Fig. S18 The depth of field map of density distribution of C_2H_4 (a), C_2H_6 (b), C_3H_6 (c) and C_3H_8 (d) in **HIAM-317b** at 298K, 100 kPa.